Structural and Instrumentation Design of a MEMS Biaxial Accelerometer

TR-CIM-06-12 June, 2012

Ting Zou

Jorge Angeles

Centre for Intelligent Machines, Department of Mechanical Engineering
McGill University, Montréal, Canada

Abstract

Based on the theory of Parallel-Kinematics Machines (PKM), a novel architecture for the compliant realization of biaxial accelerometers is proposed. In this work, notched, termed Π-joints in the PKM literature, with Lamé-notched hinges serving as flexible joints, are employed. Furthermore, through comparison among different sensing technologies, piezoresistive sensing is found to be attractive and adopted in the sensor design. On the basis of piezoresistive principles, two types of electronic layouts are developed for the accelerometer, with different locations for the resistors: on the top surface and on the vertical sidewall of the notched hinge. Moreover, modal analysis results reveal that the proposed accelerometer architecture provides good compliance along the sensitive axes and high off-axis stiffness. In addition, through a piezoresistive analysis conducted using finite element software, the matrix that maps voltage signals into applied force and moment is derived. The proposed biaxial accelerometer model is proved to achieve in-plane calibration effectively.

Keywords: simplicial MEMS accelerometer, Lamé curves, piezoresistive sensing

1 Introduction

The working principle of an accelerometer relies on the mass-spring-dashpot system. In uniaxial accelerometers, the mass, which is referred to as the *proof-mass*, can translate along one direction, termed the *sensitive axis*, with the help of a viscoelastic suspension. The accelerometer is rigidly mounted on a moving body $\mathcal{B}$ whose acceleration is to be measured; then, the resulting displacement of the proof-mass yields a signal which obeys a linear relation with the acceleration [1]. In microaccelerometers, the viscoelastic suspension is commonly realized by the entrapped air or fluid added to the damping, which is provided by the material. In the case of multiaxial accelerometers, a pure translation of the proof-mass with respect to $\mathcal{B}$ is required [2].

With rapid progress in MEMS (Microelectromechanical Systems) technologies, microaccelerometers have been the subject of intensive research. Actually, microacclerometers are distinguished due to their compactness, robust sensing, relative low cost and extensive commercial use in automotive and industrial applications [3]. Acceleration measurement is one important application of accelerometers; for example, accelerometers can be used as components in GPS-aided inertial navigation systems. Furthermore, accelerometers for tilt measurements can also be integrated into a multitude of products, such as 3D mice, cameras and personal navigation systems. In addition, twist—velocity and angular velocity—and its time-rate of change can also be estimated with accelerometers, arrayed in what is known as *accelerometer strapdowns* [4]. The wide application of accelerometer arrays include crashworthiness, gait analysis and vehicle navigation, among others [5, 6, 7].

According to Maluf [8], all accelerometers share a basic structure, consisting of a proof-mass mounted on a moving body by means of a viscoelastic suspension. However, they differ in the sensing of the relative position of the proof-mass, as the mass translates relative to the accelerometer frame under the effect of a rigid-body acceleration. Measurement techniques for the estimation of proof-mass displacements have been reported, including measurement methods based on piezoelectricity, metallo-resisitivity, capacitance, piezoresistivity, optical sensing mechanisms based on diffraction-gratings, and optical microencoders [9]. Among them, the piezoelectricity and metallo-resisitivity are widely used in high-frequency applications: the piezoelectricity is mainly employed for vibration measurements, while the metallo-resisitivity is characterized by low temperature drift, low noise and high precision. On the contrary, the capacitance and piezoresistivity are mainly used physical principles for low-frequency applications. Commonly known as optical detection techniques, the optical sensing mechanisms based on diffraction-gratings and optical microencoders also have a wide range of applications. Actually, in comparison with capacitive and piezoresistive technologies, the optical detection techniques are well acknowledged due to their high sensitivity [10]. A summary of characteristics of different sensing technologies is given in Table 1. Among different sensing technologies, the piezoresistive sensing is attractive because it relies on a compact mechanism that requires neither complex processing circuitry nor a bulky external apparatus, besides exhibiting low susceptibility to electromagnetic interference.

In this paper, a novel design of the compliant realization of biaxial accelerometer structure is carried out. Both the conceptional and structural design are presented, with the goal of increasing off-axis stiffness. Piezoresistive sensing is combined with the accelerometer mechanical architecture to implement in-plane calibration. In order to validate the electronics layout, a new approach

Table 1: Comparison among characteristics of different sensing technologies

Specifications	Piezoelectric	Piezoresistive	Capacitive
Output impedance	High	Low	High
DC response	No DC response	Can measure down to DC, *e.g.* throughout long-duration events such as those associated with automobile braking	Can measure down to DC
Power consumption	Self-generating	Require an external power source	Require a standard voltage supply or battery
Temperature range	Large	Small	Very large
Sensitivity	Medium	Medium	High
Offset drift	Offset drift with impact	Offset drift with temperature	None
Complexity of circuitry	Medium	Low	High
Application ranges	Vibration measurements, *i.e.*, higher frequency	low-frequency applications	Wide bandwidth, low-frequency applications
Cross-axis sensitivity	Mainly determined by accelerometer mechanical design		
Advantages	Relatively small size, large bandwidth, high resonant frequency, good linearity	Simplicity of design, fabrication process and processing circuitry; compactness	High sensitivity, low power consumption, broad bandwidth, good linearity and stability
Disadvantages	No DC-response, high leakage	Temperature sensitivity	Relatively high cost, electromagnetic interference

including the mapping matrix is investigated, which is also interesting for general sensing analysis for accelerometers.

2 Conceptional Design

2.1 Simplicial Architectures for Multi-axial Accelerometers

Based on the concepts of Parallel-Kinematics Machines, novel simplicial[1] architectures for multi-axial accelerometers were proposed by Cardou [4], in which the proof-mass was suspended by $n+1$ legs ($n = 1, 2, 3$), where n is the number of acceleration components measurable by the accelerometer. Hence, in n-dimensional space, for $n = 1, 2, 3$, the simplex is a line segment, a triangle and a tetrahedron, respectively. Having one extra leg offers redundancy in the measurement, thereby providing robustness against measurement error.

The Π-joint is a parallelogram four-bar linkage, which allows for pure translation between two opposite links: all the points of one describe circles, of variable location and radius identical to the length of the two other links, on the other. It is noted that the $\Pi\Pi\Pi$ leg is a generator of $\mathcal{T}_2$, a rigid-body-motion subgroup, characterized by pure translations along the directions of two distinct unit vectors.

The simplicial uniaxial accelerometer (SUA) shown in Fig. 1(a) is intended to measure point-acceleration along one direction, the horizontal in that figure; the accelerometer is realized by means of two opposing $\Pi\Pi\Pi$ legs lying in orthogonal planes to constrain the proof-mass to translate in a direction parallel to the line of intersection of the two planes. Its biaxial counterpart (SBA), a planar parallel mechanism, as shown in Fig. 1(b), is realized by laying out the three $\Pi\Pi\Pi$ legs in a common plane at 120° from one another. The SBA allows arbitrary translations parallel to the said plane, while providing a high stiffness along the direction perpendicular to the plane. Finally, the

[1]The term derives from *simplex*, a polyhedron with the minimum number of vertices embedded in $\mathbb{R}^n$ [11].

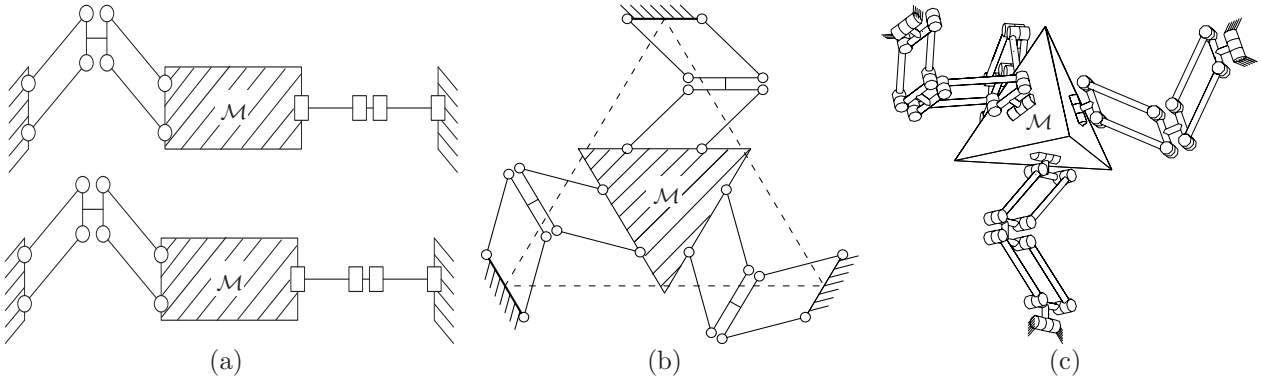

Figure 1: Layout of simplicial accelerometers: (a) SUA; (b) SBA; (c) STA

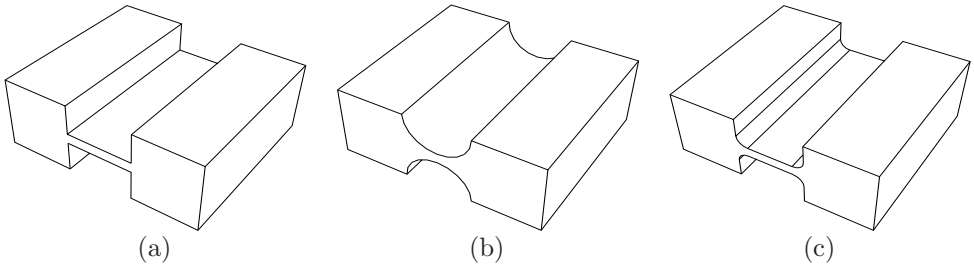

Figure 2: General realization of flexure hinges: (a) leaf type; (b) circular-notched; and (c) corner-filleted

simplicail triaxial accelerometer (STA) is achieved by suspending a regular tetrahedral proof-mass by means of four $R\text{III}R$ legs, as shown in Fig. 1(c). The STA has a parallel-robot architecture which allows pure translations of the proof-mass with respect to the frame.

In this work, we focus on the compliant realization of the SBA, which can be done by means of microfabrication technology due to its planar nature.

2.2 Compliant Mechanisms and Design of Flexure Hinges

Within the framework of Lobontiu [12], compliant mechanisms are flexure-based monolithic structures, in which flexure hinges are commonly employed to produce a desired motion, rather than conventional joints—those realizing lower and higher kinematic pairs [13]. Therefore, a compliant mechanism comprises at least one component that is highly deformable (compliant) as compared to the other links. In comparison with conventional rigid-body mechanisms, the compliant mechanisms may have many desirable features: no assembly needed; no backlash; compactness; low cost; and wear-resistance, since they are jointless [14]. This jointless intrinsic factor distinguishes the compliant mechanisms from the rigid-body mechanisms, which employ lower pairs such as pins and sliders. On the other hand, due to the complexity and nonlinearity of flexure hinges, the design and fabrication of compliant mechanisms is always extremely difficult [15]. Moreover, a few challenges companion due to the jointless feature, first and foremost, a limited range of motion [16]. In addition, the precision of rotation of flexure hinges is affected due to the complex

deformation of the flexure.

The application of flexure-based compliant mechanisms has drawn a lot of attentions during the past years, especially in microscale devices [17, 18]. A few examples include micro-positioning systems, microsensors, tilt mirrors, and microfluidic devices. Among them, the two-dimensional application of flexure hinges is employed in a wide range of different fields, for example, the MEMS devices. With reference to Lobontiu [12], this kind of hinge is supposed to be compliant only about one axis (the sensitive axis), and stiff (as much as possible) about all other directions of possible motion.

The general realization of flexure hinges depends on the cross-section profile; some of the common configurations are illustrated in Fig. 2. In this design, flexure hinges for two-dimensional applications are used.

The realization of compliant Π-joints is shown in Fig. 3. One possibility is by means of one pair of long beams with constant cross-section, another being by means of four notched hinges, as illustrated in Fig. 3 (a) and (b), respectively. As mentioned above, the notched Π-joint has the desirable feature of high stiffness ratios between the sensitive direction and the other directions. However, this type of realization exhibits the inherent demerit of a limited range of motion.

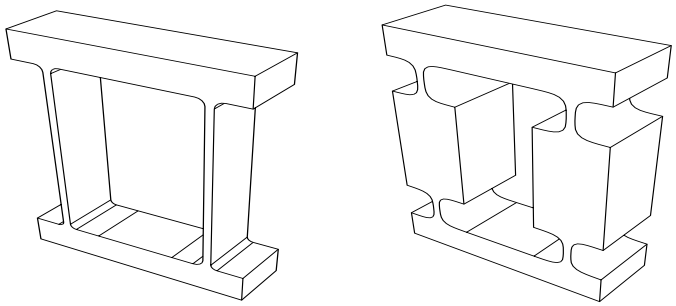

(a) (b)

Figure 3: Compliant realization of the Π-joint with: (a) a pair of long beams; (b) four notched hinges

3 Structural Design

Instead of using the Π-joint with a pair of constant cross-section beams, as shown in Fig. 3(a), notched Π-joints, as depicted in Fig. 3(b), are employed in our realization of the SBA. A static analysis in ANSYS revealed that the SBA architecture with three Π-joints of the type shown in Fig. 3(a) entails a problem of interference between the proof-mass and the fixed frame, due to the high compliance of the structure. In order to overcome this deficiency, an improved 3ΠΠ layout is proposed, as illustrated in Fig. 4. For accelerometers, the Lamé-notched flexure hinge is a good choice for the construction of notched Π-joint [19]. In this design, the notched Π-joint is realized by means of Lamé-notched flexure hinge, with minimum thickness $t_m = 20$ μm, length $l = 210$ μm, along with the two design parameters of a 4th-order Lamé curve: $a_x = 105$ μm and $a_y = 70$ μm. The geometry of the Lamé-notched flexure hinge is depicted in Fig. 5.

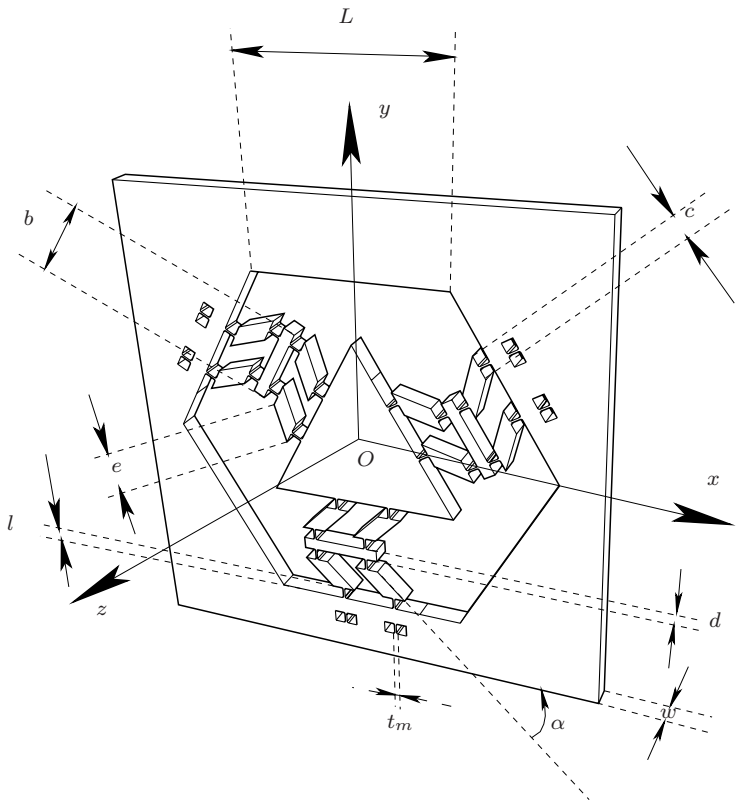

Figure 4: SBA design with its dimensions

Silicon is widely used for fabrication of semiconductor devices. Here, the material used for this model is single-crystal silicon. The values of the model parameters and material properties of silicon are listed in Tables 2 and 3, respectively.

Table 2: Dimensions of the SBA

a (μm)	b (μm)	c (μm)	d (μm)	e (μm)	l (μm)	L (μm)	t_m (μm)	α	w (μm)
3333	1400	200	210	700	210	3466	20	$\pi/4$	300

4 Electronics Layout

4.1 Piezoresistive Principle

The piezoresistive effect is a phenomenon that changes the resistance of a material under applied stresses. This effect results from both geometric changes and the change in resistivity, which is given by Richter et al. [20]:

$$\frac{\Delta R}{R} = (1 + 2\nu)\epsilon + \frac{\Delta \rho}{\rho} \tag{1}$$

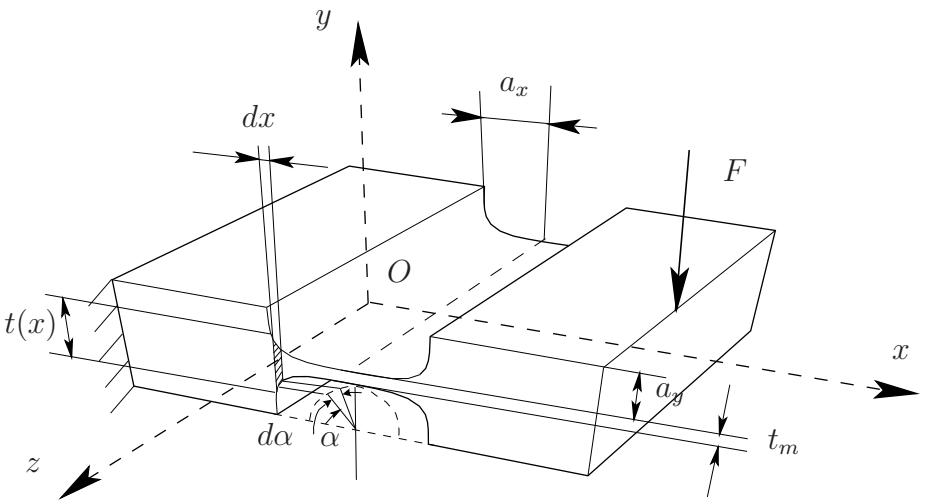

Figure 5: Geometry of a Lamé-notched flexure hinge

Table 3: Mechanical properties of silicon

Density	Stiffness Coefficients (10^3 MPa)			Young Modulus (10^3 MPa)			Poission Ratio
(kg/μm^3)	C_{11}	C_{12}	C_{13}	[100]	[110]	[111]	
2.33×10^{-15}	165.7	63.9	79.6	129.5	168.0	186.5	0.222

where ν is the Poisson ratio, ϵ is the strain along the piezoresistor, while R and ρ are resistance and resistivity, the former in the unstressed material. For semiconductor gauges, such as silicon and germanium, the changes in resistivity $\Delta\rho/\rho$ are dominant when compared with the dimensional changes in eq. (1). Hence, we can write $\Delta R/R = \Delta\rho/\rho$.

The piezoresistive effect is described by a fourth-rank tensor that relates the change in resistivity to the stress [21]. For crystals with cubic symmetry, such as silicon, the piezoresistance tensor is given, in matrix form, by

$$\frac{1}{\rho}\begin{bmatrix}\Delta\rho_1\\ \Delta\rho_2\\ \Delta\rho_3\\ \Delta\rho_4\\ \Delta\rho_5\\ \Delta\rho_6\end{bmatrix} = \begin{bmatrix}\pi_{11} & \pi_{12} & \pi_{12} & 0 & 0 & 0\\ \pi_{12} & \pi_{11} & \pi_{12} & 0 & 0 & 0\\ \pi_{12} & \pi_{12} & \pi_{11} & 0 & 0 & 0\\ 0 & 0 & 0 & \pi_{44} & 0 & 0\\ 0 & 0 & 0 & 0 & \pi_{44} & 0\\ 0 & 0 & 0 & 0 & 0 & \pi_{44}\end{bmatrix}\begin{bmatrix}\sigma_1\\ \sigma_2\\ \sigma_3\\ \sigma_4\\ \sigma_5\\ \sigma_6\end{bmatrix} \tag{2}$$

Note that the piezoresistance coefficients depend on crystal orientation, impurity concentration and temperature [22].

The relation between the electric field and the current density is

$$\begin{bmatrix}\varepsilon_1\\ \varepsilon_2\\ \varepsilon_3\end{bmatrix} = \begin{bmatrix}\rho+\Delta\rho_1 & \Delta\rho_6 & \Delta\rho_5\\ \Delta\rho_6 & \rho+\Delta\rho_2 & \Delta\rho_4\\ \Delta\rho_5 & \Delta\rho_4 & \rho+\Delta\rho_3\end{bmatrix}\begin{bmatrix}j_1\\ j_2\\ j_3\end{bmatrix} \tag{3}$$

where ε_i and j_i, $(i = 1, 2, 3)$ are the electric field and current density components along three mutually orthogonal directions, respectively.

For the piezoresistive analysis, it is necessary to transform the piezoresistive equations from one coordinate frame to another. The general expression for the longitudinal and transverse piezoresistance coefficients for a gauge in an arbitrary crystal direction is given by Mason and Thurston [23]:

$$\begin{aligned}\pi_l &= \pi_{11} - 2(\pi_{11} - \pi_{12} - \pi_{44})(l_1^2 m_1^2 + l_1^2 n_1^2 + m_1^2 n_1^2) \\ \pi_t &= \pi_{12} + (\pi_{11} - \pi_{12} - \pi_{44})(l_1^2 l_2^2 + m_1^2 m_2^2 + n_1^2 n_2^2)\end{aligned} \tag{4}$$

where (l_1, m_1, n_1) is the set of direction cosines between the longitudinal orientation and the crystal axis; (l_2, m_2, n_2) is its transverse counterpart. The resistance change is described by

$$\frac{\Delta R}{R} = \pi_l \sigma_l + \pi_t \sigma_t \tag{5}$$

where σ_l and σ_t are the longitudinal and transverse stress components.

4.2 Measurement Circuit

It is assumed that the piezoresistors are located on the SBA surface with submicrometric thickness. These resistors are p-type silicon pieces with resistivity and piezoresistance coefficients listed in Table 4, assuming a doping concentration under 10^{17} cm^{-3}.

Table 4: Piezoresistance coefficients for p-type silicon (Room temperature)

Resistivity (Ω-cm)	Piezoresistance (10^{-11}Pa^{-1})		
	π_{11}	π_{12}	π_{44}
7.8	6.6	−1.1	138.1

Two approaches to locate the resistors are considered: a) on the top surface of the notched hinge, near the edge, and b) on the vertical sidewall of the hinge, covering the top 1/3 area. For case a), the resistor has a 120-μm length and 4-μm width; for case b), the resistor is designed so as to have dimensions of 120×100 μm, since more space is available in this layout.

As shown in Fig. 6(a), three measurement circuits are employed to provide voltage signals to detect the loading in an arbitrary direction in the Oxy plane. Each of the three circuits consists of four resistors connected via a half-Wheatstone bridge, as shown in Fig. 6(b). Taking bridge I as an example, resistors R_1 and R_2 are employed as two active Wheatstone bridge elements, which are subject to opposite stress conditions. Furthermore, the two extra notched hinges formed on the accelerometer frame have the same structure as the two other hinges, which helps shape the two fixed bridge elements R_3 and R_4. Figure. 6(a) illustrates the circuit connection for bridge I for the top-surface implantation case, with the bridge drive voltage $V_s = 5V$. The connections for the other two bridges and for the vertical sidewall layout are equivalent to bridge I. It is noted that the four resistors forming a Wheatstone bridge have the same geometry, in order to provide zero-offset output voltage. At the same time, primary temperature compensation is also achieved.

Assuming that all four resistors have equivalent resistance R when no loading is applied, then, we can write

$$R_1 = (1 + \alpha_1)R, \quad R_2 = (1 - \alpha_2)R, \quad R_3 = R_4 = R \tag{6}$$

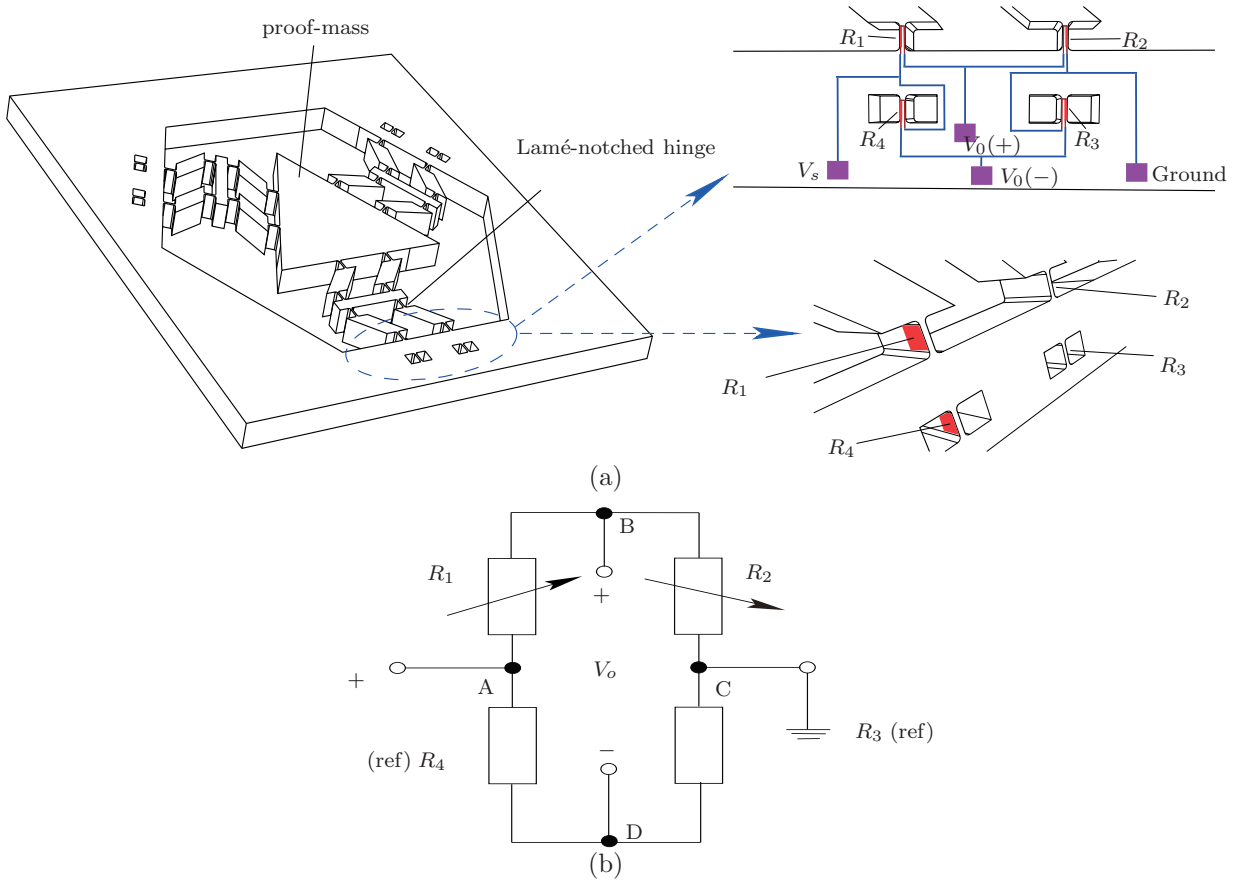

Figure 6: SBA design and sensing system: (a) measurement circuit; (b) half-Wheatstone bridge

where α_1 and α_2 are change rates of R_1 and R_2.

Hence, the resulting relation between the input and output voltages becomes

$$\frac{V_o}{V_s} = \frac{R_1}{R_1 + R_2} - \frac{R_4}{R_3 + R_4} = \frac{R_1 - R_2}{2(R_1 + R_2)} = \frac{\alpha_1 + \alpha_2}{2(2 + \alpha_1 - \alpha_2)} \tag{7}$$

As known in the art of [24], α_1 and α_2 are typically small, and differ from each other by only 10%, the input-output ratio of the half-bridge being one-half of that for the full bridge, without a large nonlinearity. Under the assumption that R_1 and R_2 are subject to the same strain value with opposite signs, the voltage ratio becomes $V_o/V_s = \Delta R/2R$.

The SBA structure starts from the n-type (100) single crystal silicon wafer. For bridge I, the resistors are oriented along the $< 1\bar{1}0 >$ direction, which gives the maximum value for π_l. The x'- and y'-axes shown in Fig. 6(a) denote the crystal axes of symmetry of the wafer. The resistors in the other two bridges are aligned along the length direction of their corresponding hinges. Then, according to eq. (4), the piezoresistance coefficients for resistors of the three Wheatstone bridges are calculated, as listed in Table 5, considering the two distinct layouts of resistor location.

Table 5: Piezoresistance coefficients for top and sidewall located resistors

Resistor location	Category	Bridge I	Bridge II	Bridge III
Top surface	(l_1, m_1, n_1)	$(-\sqrt{2}/2, \sqrt{2}/2, 0)$	$(\cos 15°, \cos 75°, 0)$	$(\cos 105°, \cos 195°, 0)$
	(l_2, m_2, n_2)	$(\sqrt{2}/2, \sqrt{2}/2, 0)$	$(\cos 75°, \cos 165°, 0)$	$(\cos 15°, \cos 105°, 0)$
	π_l (10^{-11}Pa^{-1})	71.8	22.9	22.9
	π_t (10^{-11}Pa^{-1})	-66.3	-17.4	-17.4
Vertical sidewall surface	(l_1, m_1, n_1)	$(-\sqrt{2}/2, \sqrt{2}/2, 0)$	$(\cos 15°, \cos 75°, 0)$	$(\cos 105°, \cos 195°, 0)$
	(l_2, m_2, n_2)	$(0, 0, 1)$	$(0, 0, 1)$	$(0, 0, 1)$
	π_l (10^{-11}Pa^{-1})	71.8	22.9	22.9
	π_t (10^{-11}Pa^{-1})	-1.1	-1.1	-1.1

5 Model Validation

5.1 Procedure for Obtaining the Mapping Matrix

For simple rectangular cantilevers, closed-form expressions for the stress occurring at the point of interest in terms of structure parameters are readily derived, from which the resistance changes can be obtained, as described in [24, 25]. However, for more complex architectures, finite element modelling has been found to be an effective tool. Hence, for the SBA model, two types of analysis are conducted in ANSYS, modal and static. Moreover, the piezoresistive analysis, which belongs to coupled-field analysis, is implemented by static analysis, using the element type SOLID73 (3D, 8-node brick element) to simulate the SBA structure, while PLANE223 (2D, 8-node coupled-field element) is adopted to simulate the piezoresistors. In each static analysis, the four piezoresistors are connected via a half-Wheatstone bridge, as illustrated in Fig. 6(b).

Compared with conventional piezoresistive accelerometers, the SBA model provides redundancy on signal detection, i.e., three voltage measurements are generated from an arbitrary in-plane acceleration signal, which can be decomposed into the x- and y-directions. Furthermore, in order to discern the magnitude and direction of the applied loading from the three voltage measurements directly, a corresponding mapping matrix is derived. The procedure for obtaining this matrix is explained below:

- Apply three different in-plane loading conditions: $F_x = 1\text{N}$; $F_y = 1\text{N}$; and $M_z = 1\,\text{N}\,\text{mm}$, with the force acting at the centre of mass of the proof-mass.

- Conduct a finite element analysis for each loading case and obtain the three output voltages from the Wheatstone bridges. Let

$$\mathbf{v}_x = \begin{bmatrix} v_{x_1} & v_{x_2} & v_{x_3} \end{bmatrix}^T, \quad \mathbf{v}_y = \begin{bmatrix} v_{y_1} & v_{y_2} & v_{y_3} \end{bmatrix}^T, \quad \mathbf{v}_z = \begin{bmatrix} v_{z_1} & v_{z_2} & v_{z_3} \end{bmatrix}^T \tag{8}$$

  where v_{x_i}, v_{y_i}, and v_{z_i} $(i = 1, 2, 3)$ denote ith readout of the measurement circuit under F_x, F_y and M_z, individually.

- For a general load,

$$\mathbf{w} = \begin{bmatrix} F_x & F_y & M_z \end{bmatrix}^T, \quad \mathbf{s} = \begin{bmatrix} u_x & u_y & \theta_z \end{bmatrix}^T, \quad \mathbf{w} = \mathbf{K}\mathbf{s} \tag{9}$$

where $\mathbf{s}$ is a "small"-amplitude displacement, with u_x and u_y denoting the "small" translational displacements along the x and y directions, θ_z the "small" angular displacement about the z axis; $\mathbf{K}$ denotes the 3×3 in-plane system stiffness matrix obtained from ANSYS.

Let $\mathbf{s} = \mathbf{T}\mathbf{v}$, where $\mathbf{T}$ is the 3×3 matrix that maps the voltage readouts shown in eq. (8) onto $\mathbf{s}$. Then, substituting this equation into eq. (9) yields

$$\mathbf{K}^{-1}\mathbf{w} = \mathbf{T}\mathbf{v} \tag{10}$$

The nine entries of $\mathbf{T}$ are obtained from the equations derived upon substituting eq. (8) into eq. (10). Then, $\mathbf{R} = \mathbf{T}^{-1}$ is obtained, which satisfies $\mathbf{v} = \mathbf{R}\mathbf{s}$.

- According to eq. (10),

$$\mathbf{w} = \mathbf{Q}\mathbf{v}, \quad \mathbf{Q} = \mathbf{K}\mathbf{T}, \quad \mathbf{v} = \mathbf{Q}^{-1}\mathbf{w} = \mathbf{P}\mathbf{w}, \quad \mathbf{P} = \begin{bmatrix} \mathbf{v}_x & \mathbf{v}_y & \mathbf{v}_z \end{bmatrix} \tag{11}$$

where matrix $\mathbf{P}$ relates the applied loading $\mathbf{w}$ with the readout $\mathbf{v}$.

5.2 Modal Analysis

Modal analysis was conducted to obtain the first six natural frequencies and mode shapes of the structure, with the results listed in Table 6.

Table 6: Modal analysis of the SBA model

i	1	2	3	4	5	6
f_i(kHz)	3.3149	3.3311	5.4356	11.558	11.570	11.682
Mode shape[1]	T_y	T_x	T_z	R_y	R_x	R_z

[1] T_i $(i = x, y, z)$ denotes translation along the i-axis; R_i $(i = x, y, z)$ is rotation about the i-axis.

Table 6 indicates that the natural frequencies f_1 and f_2, which correspond to translations in the plane, along the y- and x-axis, respectively. In addition, it is noticeable that the natural frequencies of out-of-plane translation and rotational motions are higher than those of in-plane translations; in particular, the rotational modes show frequency values three times as high as their in-plane counterparts.

5.3 Piezoresistive Analysis

First, a set of simulations is conducted to obtain the output voltage of bridge I in the vertical sidewall case, considering the values of the applied forces F_x and F_y continuously increasing. The relation between the applied loading and the output voltage are plotted in Fig. 7, where the scattered points are simulation results obtained from ANSYS, while the straight line is generated by a linear fit.

From Fig. 7 it is apparent that the output voltage obeys a linear relation with the applied loading. The least-square errors for these two linear fits are 0.0672% and 0.0223%, respectively.

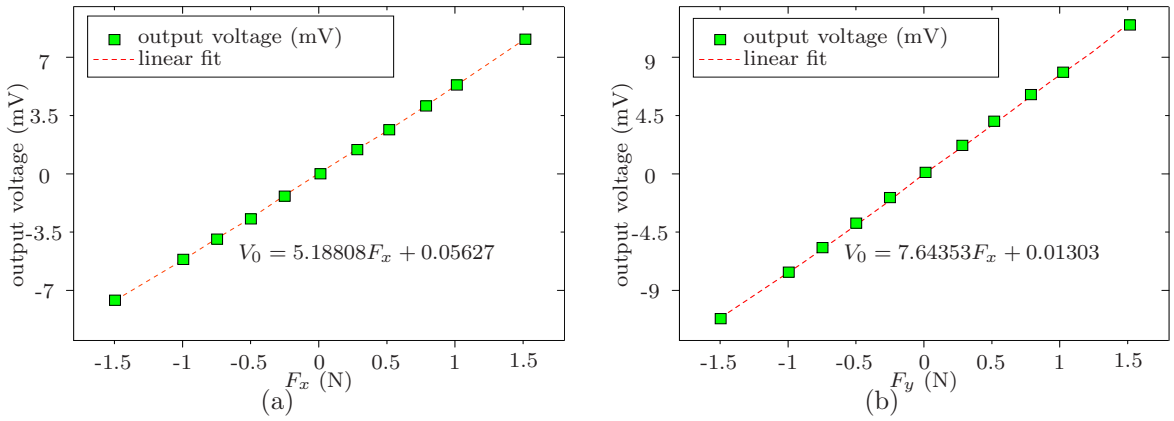

Figure 7: The relationship between the applied loading and the generated voltage: (a) F_x; (b) F_y

Furthermore, simulations are implemented to find the mapping matrices that relate the three output measurements with the displacement, and the voltage measurements with the applied loading.

With reference to Fig. 4, the in-plane stiffness matrix for the whole system, as reported by ANSYS, is:

$$\mathbf{K} = \begin{bmatrix} 45.7198 & 3.8745 \times 10^{-3} & 4.0021 \times 10^{-3} \\ 3.8745 \times 10^{-3} & 45.8711 & 9.1863 \times 10^{-3} \\ 4.0021 \times 10^{-3} & 9.1863 \times 10^{-3} & 0.7650 \end{bmatrix} \tag{12}$$

whose 2×2 upper-left block has units of N/mm, its 2×1 and 1×2 off-diagonal blocks units of N/rad, and its $(3, 3)$ entry units of N mm/rad.

For the piezoresistors located on the top surface,

$$\mathbf{R} = \mathbf{T}^{-1} = \begin{bmatrix} 195.3071 & 282.6073 & 0.0227 \\ -342.9768 & 28.2190 & -0.0295 \\ 146.5107 & -311.9325 & 0.0065 \end{bmatrix}, \quad \mathbf{P} = \mathbf{Q}^{-1} = \begin{bmatrix} 4.2713 & 6.1605 & -1.0367 \times 10^{-4} \\ -7.5018 & 0.6158 & -1.0367 \times 10^{-4} \\ 3.2051 & -6.8005 & -1.0367 \times 10^{-4} \end{bmatrix} \tag{13}$$

The 3×2 left-hand block of $\mathbf{R}$ has units of mV/mm, its third column units of mV/rad, while the 3×2 left-hand block of $\mathbf{P}$ has units of mV/N, its third column units of mV/(N mm).

For piezoresistors located on the vertical sidewall surface,

$$\mathbf{R} = \mathbf{T}^{-1} = \begin{bmatrix} 241.8080 & 358.2517 & 0.0283 \\ -408.7624 & 31.1230 & -0.0352 \\ 185.0979 & -370.4622 & 0.00875 \end{bmatrix}, \quad \mathbf{P} = \mathbf{Q}^{-1} = \begin{bmatrix} 5.2883 & 7.8096 & -4.0716 \times 10^{-5} \\ -8.9407 & 0.6792 & -4.0716 \times 10^{-5} \\ 4.0492 & -8.0765 & -4.0716 \times 10^{-5} \end{bmatrix} \tag{14}$$

The above matrices have the same units as their counterparts in eq. (13). The foregoing results demonstrate that, for in-plane calibration, the Wheatstone bridge with vertical sidewall piezoresistors provide larger sensitivity than the sensing elements placed on the top surface. Furthermore, vertical sidewall piezoresistors are commonly employed for in-plane sensors [26, 27, 28].

Table 7: Validation of mapping matrices

	$\mathbf{v}'$ (mv)	$\mathbf{v}$ (mv)	MAPE
Top	$\begin{pmatrix}-2.366720786 & 15.53745777 & -13.28043391\end{pmatrix}^T$	$\begin{pmatrix}-2.382075813 & 15.61936948 & -13.21070759\end{pmatrix}^T$	0.0057
Sidewall	$\begin{pmatrix}-2.757804278 & 18.391174 & -15.98428694\end{pmatrix}^T$	$\begin{pmatrix}-2.766997431 & 18.56065200 & -16.17500793\end{pmatrix}^T$	0.0082

In order to verify the above mapping matrices, the output voltage $\mathbf{v}$ under both top and sidewall cases is evaluated according to $\mathbf{v} = \mathbf{P}\mathbf{w}$, where $\mathbf{w} = \begin{bmatrix} -2 & 1 & 0 \end{bmatrix}^T$ is one applied in-plane loading. In addition, the voltage readout $\mathbf{v}'$ from FEA, which is considered as the exact value here, is also recorded in Table 7 for comparison purposes. Furthermore, the mean absolute percentage error (MAPE) is used to compare $\mathbf{v}$ and $\mathbf{v}'$, which is given by

$$\mathrm{MAPE} = \frac{1}{\mathrm{n}} \sum_{\mathrm{i}=1}^{\mathrm{n}} \left| \frac{\mathrm{v}'_{\mathrm{i}} - \mathrm{v}_{\mathrm{i}}}{\mathrm{v}'_{\mathrm{i}}} \right| \tag{15}$$

where $n = 3$, while v_i and v'_i denote the ith entry of $\mathbf{v}$ and $\mathbf{v}'$, respectively.

6 Conclusions

On the basis of knowledge on both both Parallel-Kinematics Machines and compliant mechanism, a novel architecture of biaxial accelerometer was devised. Modal analysis was conducted, and the accelerometer model was detected to provide good compliance in the sensitive axes as well as low cross-axis sensitivity. In addition, the electronic layout was also designed, with two approaches in locating the piezoresistors: on the top surface and on the vertical sidewall of the flexure hinge. Piezoresistive analysis was adopted using FEA software to investigate these two approaches, and results reveal that both of them are effective to detect the output voltage from the measurement circuits under applied loading. Furthermore, the mapping matrices relating the applied loading to the voltage measurements are derived for the two electronic layouts. The second approach performs superior over the first one through a FE analysis.

A prototype of the SBA model will be fabricated in the near future. Also, a set of experiments will be conducted to further validate the simulation results reported here.

Acknowledgements

The support of Québec's Fonds de recherche sur la nature et les technologies through grants FQRNT PR-112531 and FQRNT PR-112531-Equip is highly acknowledged. NSERC's support through a Dsicovery Grant to each of the second and the third co-authors is also dutifully acknowledged.

References

[1] J. Becedas, G. Mamani, V. Feliu-Batlle, H. Sira-Ramírez, Algebraic identification method for mass-spring-damper system, Proceedings of the World Congress on Engineering and Computer Science, San Francisco, USA, 2007.

[2] B. V. Amini, F. Ayazi, Micro-gravity capacitive silicon-on-insulator accelerometers, Journal of Micromechanics and Microengineering 15 (2005) 2113-2120.

[3] J. C. Yu, C. B. Lan, System modeling and robust design of microaccelerometer using piezoelectric thin film, Proceedings of IEEE/SICE/RSJ International Conference, Taipei, 1999.

[4] P. Cardou, Design of Multiaxial Accelerometers with Simplicial Architectures for Rigid-body Pose and Twist Estimation, Ph.D. thesis, McGill University, Montreal, Canada, 2008.

[5] R. T. Shea, D. C. Viano, Computing body segment trajectories in the hybrid iii dummy using linear accelerometer data, ASME Journal of Biomechanical Engineering 116 (1994) 37-43.

[6] M. D. Miles, Measurement of six-degree of freedom model motions using strapdown accelerometers, 21st American Towing Tank Conference, Washington DC, USA, 1986, pp. 369-375.

[7] O. E. J. Pamadi, K. B., T. R. Pepitone, Assessment of a GPS guided spinning projectile using an accelerometer-only IMU, Proceeding of AIAA Guidance, Navigation and Control Conference and Exhibit, Providence, Rhode Island, USA, 2004, pp. 705-717.

[8] N. Maluf, An Introduction to Microelectromechanical Systems Engineering, Artech House Publishers, Boston, 2000.

[9] B. E. Boser, R. T. Howe, Surface micromachined accelerometers, IEEE Journal of Solid-State Circuits 31 (1996) 366-375.

[10] N. A. Hall, F. L. Degertekin, Integrated optical interferometric detection method for micromachined capacitive acoustic transducers, Applied Physics 80 (2002) 480-486.

[11] E. Kreyszig, Advanced Engineering Mathematics, John Wiley & Sons, New York, 1997.

[12] N. Lobontiu, Compliant Mechanisms: Design of Flexure Hinges, CRC Press: Boca Raton, FL, USA, 2003.

[13] R. S. Hartenberg, J. Denavit, Kinematic Synthesis of Linkages, McGraw-Hill, New York, 1964.

[14] H.-J. Su, A pseudorigid-body 3R model for determining large deflection of cantilever beams subject to tip loads, ASME Journal of Mechanisms and Robotics 1 (2009) 1-9.

[15] P. Bernardoni, P. Bidaud, C. Bidard, A new compliant mechanism design methodology based on flexible building blocks, Proceedings of SPIE, San Diego, CA, USA, 2004.

[16] S. Smith, Flexure Elements of Elastic Mechanisms, Gordon and Breach Science Publishers, The Netherlands, 2000.

[17] S. Shuib, M. I. Z. Ridzwan, A. H. Kadarman, Methodology of compliant mechanisms and its current development in applications: a review, American Journal of Applied Sciences 4 (2007) 160-167.

[18] V. Seidemann, S. Butefisch, S. Buttgenbach, Fabrication and investigation of in-plane compliant su8 structures for MEMS and their application to micro valves and micro grippers, Sensors and Actuators A 97-98 (2002) 457-461.

[19] S. Desrochers, Optimum Design of Simplicial Uniaxial Accelerometers, Master of engineering thesis, Department of Mechanical Engineering, McGill University, Montreal, Canada, 2008.

[20] J. Richter, O. Hansen, A. N. Larsen, J. L. Hansen, G. F. Eriksen, E. V. Thomsen, Piezoresistance of silicon and strained $Si_{0.9}Ge_{0.1}$, Sensors and Actuators (2005) 388-396.

[21] S. Sze, Semiconductor Sensors, John Wiley & Sons, New York, 1994.

[22] Y. Kanda, A graphic representation of the piezoresistance coefficients in silicon, IEEE Transactions on Electron Devices ED-29 (1) (1982) 64-70.

[23] W. P.Mason, R. N. Thurston, Use of piezoresistive materials in the measurement of displacement, force and torque, J. Acous. Soc. of Am. 29 (1957) 1096-1101.

[24] S. D. Senturia, Microsystem Design, Kluwer Academic Publishers, Norwell, MA, 2001.

[25] E. J. Eklund, A. M. Shkel, Single-mask fabrication of high-g piezoresistive accelerometers with extended temperature range, Journal of Micromechanics and Microengineering 17 (2007) 730-736.

[26] A. A. Barlian, S. J. Park, V. Mukundan, B. L. Pruitt, Design and characterization of microfabricated piezoresistive floating element-based shear stress sensors, Sensors and Actuators 134 (2007) 77-87.

[27] A. Patridge, K. Reynolds, W. Chui, A high-performance planar piezoresistive accelerometer, Journal of Microelectromechanical Systems 9 (2000) 58-66.

[28] B. K. Nguyen, K. Hoshino, K. Matsumoto, I. Shimoyama, Insertion force sensor by sidewall-doping with rapid thermal diffusion, MEMS 2006, Istanbul, Turkey, 2006, pp. 22-26.